Multi-modal 2D-3D Non-rigid Registration

M. Prümmer[a], J. Hornegger[a], M. Pfister[c], A. Dörfler[b]

[a] Institute of Pattern Recognition, University of Erlangen-Nuremberg
[b] Division of Neuroradiology University of Erlangen-Nuremberg
[c] Siemens Medical Solutions, Forchheim (Germany)

ABSTRACT

In this paper, we propose a multi-modal non–rigid 2D-3D registration technique. This method allows a non–rigid alignment of a patient pre-operatively computed tomography (CT) to few intra operatively acquired fluoroscopic X-ray images obtained with a C-arm system. This multi-modal approach is especially focused on the 3D alignment of high contrast reconstructed volumes with intra-interventional low contrast X-ray images in order to make use of up–to–date information for surgical guidance and other interventions. The key issue of non-rigid 2D-3D registration is how to define the distance measure between high contrast 3D data and low contrast 2D projections. In this work, we use algebraic reconstruction theory to handle this problem. We modify the Euler–Lagrange equation by introducing a new 3D force. This external force term is computed from the residual of the algebraic reconstruction procedures. In the multi-modal case we replace the residual between the digitally reconstructed radiographs (DRR) and observed X-ray images with a statistical based distance measure. We integrate the algebraic reconstruction technique into a variational registration framework, so that the 3D displacement field is driven to minimize the "reconstruction distance" between the volumetric data and its 2D projections using mutual information (MI). The benefits of this 2D-3D registration approach are its scalability in the number of used X-ray reference images and the proposed distance that can handle low contrast fluoroscopies as well. Experimental results are presented on both artificial phantom and 3D C-arm CT images.

Keywords: Non-Rigid 2D-3D Registration, Fluoroscopic X-ray to C-arm CT Registration, Multi-Modal Registration, Computer-Assisted Surgery

1. INTRODUCTION

1.1. Clinical Motivation

The goal of 2D-3D registration is to find the 3D transform that aligns reconstructed volumes with intra–interventional 2D images in order to make use of up–to–date information for surgical guidance and other interventions. The 2D-3D non-rigid registration is a common problem that occurs for example in minimal invasive, intra vascular and cardiac applications. One of these applications is the registration of a pre-reconstructed 3D volume (e.g. liver or head) to angiographic or fluoroscopic 2D image sequences that are acuired during the intervention where the patient is breathing or moving. After registration, the pre-reconstructed 3D volume can be overlayed with fluoroscopic images to align the volume rendered 3D image with a catheter tip shown in the fluoroscopy. The benefit of this multi-modal approach is that high contrast 3D data can be aligned with noisy low contrast X-ray images, like fluoroscopies.

1.2. State-Of-The-Art

Many 2D-3D registration methods are proposed in literature. According to the distance measure, common methods can be roughly classified into feature- or intensity–based. Feature–based approaches make use of landmarks (fiducial or natural) or other anatomical features to match images. For example, Gueziec *et. al.*[4] use surface features to align CT volume with fluoroscopy X-ray. Feldmar et al.[5] presented a unified framework for registration of curves and surfaces. Hamadeh et al.[6] extended Feldmar's method by combining segmentation result of X-ray images. Intensity–based registration measure the similarity of intensity directly. Thus, no feature extraction is required and the whole registration procedure can be automated. E.g., Weese *et. al.*[7]

Further author information:
[a] E-mail: {pruemmer, hornegger}@informatik.uni-erlangen.de

Medical Imaging 2006: Image Processing, edited by Joseph M. Reinhardt, Josien P. W. Pluim,
Proc. of SPIE Vol. 6144, 61440X, (2006) · 0277-786X/06/$15 · doi: 10.1117/12.652321

presented an intensity–based method for 2D-3D registration. LaRose et al[8] investigate real time iterative X-ray/CT registration techniques. Zollei *et. al.*[9] employ mutual information as similarity measure and a stochastic gradient ascent approach as optimization procedure in registration problems. Yao *et. al.*[10] proposed an affine 2D-3D registration method based on a statistical model. S. Jonić, P. Thévenaz *et. al.*[23] introduced a multi-resolution spline-based 2D-3D alignment of CT volume and C-arm images for computer-assisted surgery.
Most of the prior work focused on parameterized transformation, such as rigid or affine transformation, i.e., the spatial transforms are defined by a set of parameters. However, in many clinic applications, it is more reasonable to describe the spatial transformations with a non–parameterized model, i.e., the displacement field.
The paper is organized as following: First, we introduce a mono-dimensional non–rigid registration method and step through the world of algebraic reconstruction technique (ART). Then, we combine these two techniques in a uniform framework to handle the 2D-3D multi-modal registration problem. Finally, we verify our approach via experiments on two phantoms and a C-arm CT thorax image with a synthetic deformation.

2. INTRODUCTION TO NON-RIGID REGISTRATION

In this section we briefly introduce the framework of the intensity–based non-rigid registration of same dimensional images. Here, two volumetric data are given, template volume T and reference volume R with $R, T : \Omega \mapsto \mathbb{R}$ where $\Omega :=]0,1[^d$ and $T(\boldsymbol{x})$ is the intensity value at the spatial point $\boldsymbol{x}$. For simplification, the intensities of image data have been scaled into $]0,1[$.

2.1. Mono-dimensional Registration

The mathematical description of the mono–dimensional registration problem is to find a displacement field $\boldsymbol{u} : \mathbb{R}^d \to \mathbb{R}^d$, such that

$$\mathcal{J}[\boldsymbol{u}] := \mathcal{D}[R, T; \boldsymbol{u}] + \alpha \mathcal{S}[\boldsymbol{u}] = \min \tag{1}$$

The *distance measure* $\mathcal{D}$ indicates the dissimilarity between the two volumes. E.g., the *sum of squared differences* (SSD) is one of the most popular distance measures for monomodal registration problems. The *regularizer* $\mathcal{S}$ in (1) is added as the remedy for the arbitrary irregularity of transformation. They are defined as:

$$\mathcal{D}^{\mathrm{SSD}}[R, T; \boldsymbol{u}] := \frac{1}{2}\int_\Omega (T_{\boldsymbol{u}}(\boldsymbol{x}) - R(\boldsymbol{x}))^2 \, d\boldsymbol{x} \quad \text{and} \quad \mathcal{S}^{curv}[\boldsymbol{u}] := \frac{1}{2}\sum_{l=1}^{d}\int_\Omega (\Delta \boldsymbol{u}_l(\boldsymbol{x}))^2 \, d\boldsymbol{x} \tag{2}$$

and $T_{\boldsymbol{u}}(\boldsymbol{x})$ denotes the deformed template volume $T(\boldsymbol{x} - \boldsymbol{u}(\boldsymbol{x}))$. Many regularizers have been proposed in the literature e.g. Modersitzki,[15] Fischer,[15] Hermosillo,[2] Chefd' Hotel,[2] Broit[11] *et. al.*. Here, we employ the *curvature regularizer*. According to the theory of variational calculus, the optimal $\boldsymbol{u}$ in (1) is characterized by the related Euler–Lagrange equation

$$\boldsymbol{f}_{\boldsymbol{u}}(\boldsymbol{x}) + \alpha \Delta^2[\boldsymbol{u}](\boldsymbol{x}) = 0. \tag{3}$$

$\boldsymbol{f}_{\boldsymbol{u}}(\boldsymbol{x})$ is so-called external force term, which is computed from the intensity of images after transformation. It drives the algorithm to search for the optimal displacement $\boldsymbol{u}$ that aligns images. Mathematically, $\boldsymbol{f}_{\boldsymbol{u}}(\boldsymbol{x})$ is the Gâteaux derivative of the distance measure $\mathcal{D}$ in (1).

2.2. Mono-dimensional Image Distance

For the SSD distance measure, the force can be computed as following,

$$\boldsymbol{f}_{\boldsymbol{u}}(\boldsymbol{x}) = D^I_{\boldsymbol{u}}(\boldsymbol{x}) \cdot \nabla T_{\boldsymbol{u}}(\boldsymbol{x}) \tag{4}$$

Here $\nabla T_{\boldsymbol{u}}$ is the gradient vector field of transformed image. It contains the structure information of the underlying objects and determines the direction of the force term. $D^I_{\boldsymbol{u}}(\boldsymbol{x}) = (R(\boldsymbol{x}) - T_{\boldsymbol{u}}(\boldsymbol{x}))$ is the *variational gradient* of the SSD based dissimilarity functional as shown by Hermosillo, Chefd' Hotel *et. al.*[2] and in this case it is the difference of two images' intensities. It can be understood as a signed distance between $[-1, 1]$. If two

mono–modal images are to be aligned, this factor $D^I_{\boldsymbol{u}}(\boldsymbol{x})$ will approach to 0 and the force will nearly vanish. An $\mathcal{O}(N \log N)$ numerical scheme (time-marching, DCT-technique) for equation (3) was designed by Fischer[15] and Modersitzki[15] . For multi-modal image registration the variational gradient can easily be modified also for statistical dissimilarity functionals like *Cross Correlation* and *Mutual Information.* A comparison of different dissimilarity functionals for variational methods is given e.g. by Hermosillo.[2]
The conventional mono–dimensional non–rigid registration techniques are not applicable in 2D-3D registration problem, because their distance measures - $D^I_{\boldsymbol{u}}(\boldsymbol{x})$ for SSD - fail to express the dissimilarities between a 3D volume and 2D projections. Therefore we replace $D^I_{\boldsymbol{u}}(\boldsymbol{x})$ with a new 2D-3D disssimilarity measure.

3. NON–RIGID 2D-3D REGISTRATION

The 2D-3D registration can be defined as following. We have the floating volume $T_{\boldsymbol{u}}(\boldsymbol{x})$ and a number of 2D projections R^{ϕ}'s. Here $\phi = 0, ..., \Phi$ and Φ is the number of projections. Given the projection model, the task of non-rigid 2D-3D registration is to find the 3D displacement $\boldsymbol{u}$ that aligns the volume $T_{\boldsymbol{u}}(\boldsymbol{x})$ to the 2D projections R^{ϕ}'s. In order to solve 2D-3D registration under variational framework, we need to find a proper distance, let's say $D^R_{\boldsymbol{u}}(\boldsymbol{x})$, to take place the $D^I_{\boldsymbol{u}}(\boldsymbol{x})$ in (4), which describes the dissimilarity between the 2D-3D images. Such a distance needs to fulfill the following criterions: $D^R_{\boldsymbol{u}}(\boldsymbol{x})$ must be bounded, the value of $D^R_{\boldsymbol{u}}(\boldsymbol{x})$ can indicate a signed distance between $T_{\boldsymbol{u}}(\boldsymbol{x})$ and R^{ϕ}'s and if the R^{ϕ}'s are the projections of the $T_{\boldsymbol{u}}(\boldsymbol{x})$, $D^R_{\boldsymbol{u}}(\boldsymbol{x}) = 0$.
In this paper we propose 3D reconstructed *residuals* between 2D projections and 3D volume as this signed distance, based on statistical dissimilarity functionals. Pure intensity based residual terms are extensively used in the iterative reconstruction approaches, e.g., Censor[17] and Gordon's[16] component averaging algebraic reconstruction scheme and others can be found in Jiang[20] and Wang[21] . Different ARTs have different residual weighting terms. But all the residuals satisfy the previous three criterion of $D^R_{\boldsymbol{u}}(\boldsymbol{x})$. In the following, we introduce the relevant knowledge about algebraic reconstruction, then present the new 3D force term based on residuals and give the overall algorithm finally.

3.1. Algebraic Reconstruction Technique

For the ease of presentation we serialize $T_{\boldsymbol{u}}(\boldsymbol{x})$ into a vector $\boldsymbol{t_u}$ according to lexicographical ordering. The projections R_{ϕ}'s are also serialized into one vector in following way:

$$\boldsymbol{r} = (\boldsymbol{r}^1, \boldsymbol{r}^2, \dots, \boldsymbol{r}^{\Phi}) = (r^1_1, \dots, r^1_m, \cdots, r^{\Phi}_1, \dots, r^{\Phi}_m)^{\top} \in \mathbb{R}^{m\Phi} \tag{5}$$

Each $\boldsymbol{r}^{\phi}$ is the lexicographical ordering vector of projection image ϕ with the ith pixel intensity r^{ϕ}_i. And m is the number of observed intensities in each projection image. The task of algebraic image reconstruction is to solve the equation system

$$\boldsymbol{A}\boldsymbol{t} = \boldsymbol{r} \tag{6}$$

(with unknown $\boldsymbol{t}$) where the $(m\Phi \times N)$-matrix $\boldsymbol{A} = (a^{\Phi}_{i,j})$ defines the projection geometry of a C-arm system or CT-scanner.

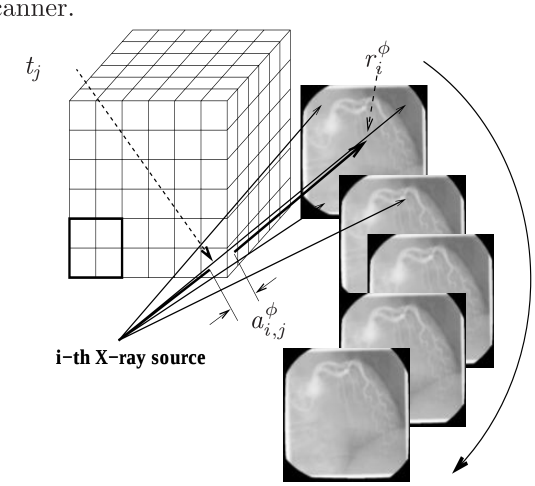

Each $a^{\Phi}_{i,j}$ element represents the contribution of the jth voxel to the ith ray during the casting of an X-ray through the human body. For each X-ray we get one of the following equations (so called *hyperplanes*):

$$\begin{aligned}
a^{\phi}_{11}t_1 + a^{\phi}_{12}t_2 + \cdots + a^{\phi}_{1N}t_N &= r_1 \\
a^{\phi}_{21}t_1 + a^{\phi}_{22}t_2 + \cdots + a^{\phi}_{2N}t_N &= r_2 \\
&\vdots \\
a^{\phi}_{M1}t_1 + a^{\phi}_{M2}t_2 + \cdots + a^{\phi}_{MN}t_N &= r_M.
\end{aligned}$$

Several *projector models*[18,22] are proposed in literature to determine the $a^{\Phi}_{i,j}$ coefficients.

Since $\boldsymbol{A}$ is large, sparse and unstructured it is not direct invertible. Several (block-)iterative solvers like *Kaczmarz, Cimmino, Censor* and *Gordon* (a convergence study and survey of the different iterative solvers is given by Jiang[21] and Wang[20]) were introduced in the past. For Kaczmarz it is shown that even in the inconsistent case of (6) the iterative solution scheme can converge towards the least square solution between all 2D projections of the reconstructed image and the observed X-ray images. In these reconstruction techniques, the intensities in image $\boldsymbol{t}$ are updated corresponding to a *relaxation residual*. The reconstruction process stops when

$$\|\boldsymbol{A}\boldsymbol{t}^k - \boldsymbol{r}\| < \epsilon \tag{7}$$

this means that the *relaxation residual* becomes small enough. The relaxation can be seen as a driving force in the reconstruction, whose value indicate scale signed "distances" between 3D image and observed projections. Ideally, when the observed 2D images are exactly the projections of the volume, the residuals on every voxels vanish. This strike property inspires us to use residuals to build up the external force for the 2D-3D registration equation.

3.2. 2D-3D Distance Measure using Mean Relaxation

To tackle the multi-dimensional distance problem of $D^I_{\boldsymbol{u}}(\boldsymbol{x})$, we use the idea of "reconstructing" the 2D dissimilarity between all corresponding projections of the floating template volume $\boldsymbol{t_u}$

$$\boldsymbol{h}^{\phi}_{\boldsymbol{u}} \quad := \quad \boldsymbol{A}^{\phi}\boldsymbol{t_u} \tag{8}$$

and X-ray images $\boldsymbol{r}^{\phi}$ into a 3D dissimilarity $D^R_{\boldsymbol{u}}(\boldsymbol{x})$ that comes from algebraic reconstruction theory. We use Censor and Gordon's[17] component averaging (CAV) technique (here, also other block-iterative ART schemes, e.g. Cimmino, are possible as well) to compute for each voxel a *dissimilarity* value to define the signed distance $D^R_{\boldsymbol{u}}(\boldsymbol{x}) \in \mathbb{R}$ and $\boldsymbol{x} \in \Omega$.

The common idea of all algebraic reconstruction techniques like ART, SART and CAV is "minimizing" the weighted back-projection of the pure intensity based 2D residual

$$\boldsymbol{d}^I_{\phi,\boldsymbol{u}} \quad := \quad \boldsymbol{r}^{\phi} - \boldsymbol{h}^{\phi}_{\boldsymbol{u}} \tag{9}$$

between all projections of the intermediate reconstruction result $\boldsymbol{t_u}$ - in our case the floating template volume - and the observed X-ray images $\boldsymbol{r}$, whereas $\boldsymbol{A}^{\phi}$ only contains the ray equations from projection ϕ. $\boldsymbol{d}^I_{\phi,\boldsymbol{u}}$ is a vector that contains for the projection angle ϕ the difference image between the observed X-ray image $\boldsymbol{r}^{\phi}$ and the projection of the deformed 3D template image with deformation $\boldsymbol{u}$. The ith element $d^I_{i,\phi,\boldsymbol{u}}$ denotes the intensity difference of the ith X-ray in the difference image for projection angle ϕ. If we serialize all 3D spatial points (voxel) $\boldsymbol{x}$ from $j = 1, \cdots, N$, the jth reconstructed signed distance $D^R_{\boldsymbol{u}}(\boldsymbol{x})$ using mean relaxation, as introduced by Prümmer, Han *et. al.*,[1] is defined as:

$$D^R_{\boldsymbol{u},j} \quad := \quad \frac{1}{\Phi}\sum_{\phi=1}^{\Phi} \frac{\sum\limits_{i=1}^{m} a^{\phi}_{i,j}\, d^I_{i,\phi,\boldsymbol{u}}}{\sum\limits_{l=1}^{n} s^{\phi}_l |a^{\phi}_{i,l}|^2}. \tag{10}$$

where s^{ϕ}_l is the number of non-zero elements (X-ray intersections of voxel l) in the lth column of $\boldsymbol{A}^{\phi}$. The pure intensity based residual $\boldsymbol{d}^I_{\phi,\boldsymbol{u}}$ in the nominator of (10) between the projection of the deformed template and the observed reference image is averaged by the components $(a^{\phi}_{i,j})$ and back-projected into 3D. $D^R_{\boldsymbol{u}}(\boldsymbol{x})$ is then the 2D-3D *mean relaxation distance* between $\boldsymbol{t_u}$ and $\boldsymbol{r}$ for all given reference images. Therefore we denote this 2D-3D distance with MRCAV. The new *relaxation force* is then defined as

$$\boldsymbol{f}^R_{\boldsymbol{u}}(\boldsymbol{x}) \quad = \quad D^R_{\boldsymbol{u}}(\boldsymbol{x}) \cdot \nabla T_{\boldsymbol{u}}(\boldsymbol{x}). \tag{11}$$

The modified Euler–Lagrange equation becomes

$$\boldsymbol{f}^R_{\boldsymbol{u}}(\boldsymbol{x}) + \alpha\Delta^2[u](x) = 0. \tag{12}$$

With such a relaxation force term, this equation characterizes the optimal 3D displacement field that minimizes the relaxation distance. At the same time, it has the same form as the original Euler-Lagrange equation of a 3D-3D registration problem. Thus, we apply the same direct DCT-technique introduced by Fischer[15] to solve the equation (12). The non–rigid 2D-3D registration algorithm is summarized as follows:

Initialization: $k \leftarrow 0, \quad \boldsymbol{u}^{(k)} \leftarrow 0$
Time Marching: $k < \mathit{maxIterations}$
Compute $D^{MI}_{\boldsymbol{u},(k)}(\boldsymbol{x})$ using (10) and (13)
Compute $\boldsymbol{f}^{MI}_{(k),\boldsymbol{u}}(\boldsymbol{x})$ using (14).
Compute $\boldsymbol{u}^{(k+1)}$ via solving (12) using $\boldsymbol{f}^{MI}_{(k),\boldsymbol{u}}(\boldsymbol{x})$.
$k \leftarrow k+1$

Figure 1. Non-rigid multi-modal 2D-3D registration

3.2.1. Sum Of Squared Difference (SSD)

For the new 2D-3D distance we replace the Gâteaux derivative $\boldsymbol{f}_{\boldsymbol{u}}(\boldsymbol{x})$ of distance measure $\mathcal{D}$ in (1) with an approximation (11). According to the convergence theorie of the block-sequencial CAV scheme[16] the computed relaxation for each voxel during the algebraic image reconstruction tells the solver the amount of intensity correction to converge overall towards (7). But in our case instead of applying this intensity correction step we deform the 3D template image $\boldsymbol{t}_{\boldsymbol{u}}$ to minimize the "reconstruction" distance in (10).
In practice different kind of 3D reconstruction algorithms for C-arm CT images are applied. Some of them apply a tissue intensity mapping from the reconstructed image intensities to real *Hounsfield* units. If we compute the forward projection of the deformed and previously intensity scaled 3D image, the $\boldsymbol{d}^{I}_{\phi,\boldsymbol{u}}$ residual between the observed fluoroscopies and the computed projections would not become zero although the images look similar even with a perfect 2D-3D alignment. The reason is that the intersection point in the consistent case of (6) of the *hyperplanes* - defined by the observed X-ray images - is not close to the solution of the pre-operatively 3D reconstructed C-arm CT image. This means a 2D-3D distance offset is observed and therefore the MRCAV distance will not be zero even if the 2D-3D alignment is perfect. If the SSD based 2D residual $\boldsymbol{d}^{I}_{\phi,\boldsymbol{u}}$ is used in (10), a proper scale of the intensities in $\boldsymbol{t}_{\boldsymbol{u}}$ is essential such that with perfect alignemt $\boldsymbol{d}^{I}_{\boldsymbol{u}}$ becomes zero.

3.2.2. Mutual Information (MI)

To overcome the mono-modal restriction of the 2D intensity based residual (9) - which corresponds to the variational gradient functional for SSD between the computed projections of the deformed template image $\boldsymbol{t}_{\boldsymbol{u}}$ and the observed low contrast X-ray images - we replace it with the variational gradient functional for MI. As shown by *Hermosillo*, *Chefd' Hotel et. al.*[2] the variational gradient for MI is given by

$$\boldsymbol{d}^{MI}_{i,\phi,\boldsymbol{u}} \quad := \quad -\frac{1}{m}\left(\frac{\partial_2 P_{\boldsymbol{u}}(\mathbf{i})}{P_{\boldsymbol{u}}(\mathbf{i})} - \frac{p'_{\boldsymbol{u}}(i_2)}{p_{\boldsymbol{u}}(i_2)}\right). \tag{13}$$

$\mathbf{i} \in \mathbb{R}^2$ is a pair of the corresponding intensities $(\boldsymbol{r}^{\phi}_{i}, \boldsymbol{h}^{\phi}_{i,\boldsymbol{u}})$, P the smooth discrete joint density function, its marginals $p_{\boldsymbol{u}}(i_1) = \sum_{\mathrm{R}} P_{\boldsymbol{u}}(\mathbf{i})di_1$ and $p_{\boldsymbol{u}}(i_2) = \sum_{\mathrm{R}} P_{\boldsymbol{u}}(\mathbf{i})di_2$ and $\partial_2 P_{\boldsymbol{u}}$ denotes the partial derivative of $P_{\boldsymbol{u}}$ with respect to its second variable. We also "reconstruct" $\boldsymbol{d}^{MI}_{\phi,\boldsymbol{u}}$ into 3D using (10) and replace for MI $\boldsymbol{d}^{I}_{\phi,\boldsymbol{u}}$ with $\boldsymbol{d}^{MI}_{\phi,\boldsymbol{u}}$. The dissimilarity measure $\boldsymbol{d}^{MI}_{\phi,\boldsymbol{u}}$ is signed and becomes zero if the intensity distributions of $\boldsymbol{r}^{\phi}$ and $\boldsymbol{h}^{\phi}_{\boldsymbol{u}} \forall \phi$ become equal. The reconstructed dissimilarity $D^{MI}_{\boldsymbol{u}}(\boldsymbol{x})$ using (10) is used for the computation of the 3D force

$$\boldsymbol{f}^{MI}_{\boldsymbol{u}}(\boldsymbol{x}) \quad = \quad D^{MI}_{\boldsymbol{u}}(\boldsymbol{x}) \cdot \nabla T_{\boldsymbol{u}}(\boldsymbol{x}). \tag{14}$$

The reconstruction of the 2D MI based dissimilarity functional to 3D provides also a solution to the Euler–Lagrange equation (12) of a common 3D-3D registration problem.

3.2.3. Generalization of Mean Relaxation

In our experiments we used the mutual information dissimilarity functional $\boldsymbol{d}^{MI}_{\phi,\boldsymbol{u}}$ for the residual between the observed X-ray images $\boldsymbol{r}^{\phi}$ and the projections $\boldsymbol{h}^{\phi}_{\boldsymbol{u}}$ of the deformed template image. The proposed residuals $\boldsymbol{d}^{I}_{\phi,\boldsymbol{u}}$ and $\boldsymbol{d}^{MI}_{\phi,\boldsymbol{u}}$ can also be replaced in the multi-dimensional case with the variational gradient of other dissimilarity functionals like *Cross Correlation* as shown for mono-dimensional registration by Hermosillo, Chefd' Hotel *et. al.*.[2]

3.3. Implementation Aspects

For the computed forward and backward projection, applied during the "mean relaxation" distance computation, several types of projectors are known. A fast, but in the sense of sampling theorem not optimal, projector is known from volume rendering techniques, the so called *alpha clipping*[19] (AC). Here, a voxel is by definition cubic and the contribution from the jth voxel to the ith X-ray is the linear intersection length of the ray and the voxel. Since we have a cone-beam projection the sampling rate of voxels that are closer to the X-ray source is higher than the one that are more distant. Using linear interpolation leads to aliasing artifacts in the computed projection image. Since our computed mean relaxation distance consists of the residuals between the observed X-ray images and the computed projections, artificial introduced 2D residuals effect the mean relaxation distance (MRCAV) by introducing ring-like artifacts. This leads to a non-smooth MRCAV distance measure.
A more sophisticated projector model is based on *interpolation kernels* (IK) like *Kaiser-Bessel* kernel. The spherical kernels overlap each other and can be adapted in their size corresponding with increasing X-ray source distance. These flexible interpolation kernels allow a adequate voxel sampling and provide a much smoother projection image compared to the AC method. But the aliasing-artifact reduction is in trade of to the computation time of the forward and backward projection. In this work we apply both the IK algorithm introduced by Müller[18] and fast AC.

4. EXPERIMENTS

First, we demonstrate the alignment of a simulated 3D cube phantom with DRRs of a sphere (Sphere-Cube). Second, we align a simulated, synthetic deformed 3D phantom (SphereHelix) to its DRRs. The DRRs are computed before the deformation. Third we use a real 3D thorax C-arm CT image , apply an artificial non-rigid deformation, and align the deformed thorax to noisy DRRs acquired before deformation.
For comparison we define the distance ϵ^{dis} between the ground truth (GT) $\boldsymbol{t}^{GT}$ - with intensity mean $\bar{t}^{GT}$ and *standard deviation* σ^{GT} - and the aligned 3D image $\boldsymbol{t}_{\boldsymbol{u}}$ as

$$\epsilon^{dis} := \frac{1}{\sigma^{GT}} \sqrt{\sum_{j=1}^{N} (\boldsymbol{t}_{j,\boldsymbol{u}} - \boldsymbol{t}^{GT}_{j})^2} \quad \text{and} \quad \sigma^{GT} > 0 \tag{15}$$

For the description of the shown experiments we introduce the following abbreviations: Volume Rendering Technique (VRT), Multiplanar Reconstruction (MPR), feed-, head-, left-, right-, anterior-, posterior-aligned MPR (MPR-F, MPR-H, MPR-L, MPR-R, MPR-A, MPR-P).
For practical application it is most important that the 2D-3D registration algorithm is robust against noisy projection images. During intervention like catheterisation only low contrast fluoroscopic images are observed to keep the X-ray dose for the patient as low as possible. A histogram equalization is applied to each single DRR and afterwards all DRRs are disturbed by Poisson noise to simulated more realistic fluoroscopies. The equalization is a non-linear intensity transformation of each single DRR. After the transformation the algebraic equation system (6) becomes highly inconsistent and makes a standard algebraic reconstruction nearly impossible. For the Sphere-Cube (Fig. 2), HelixSphere (Fig. 3, 4) and C-arm CT data (Fig. 5, 6) are several experimental cases (Table 1), e.g. different number of used X-ray images and noise level, applied.

4.1. 2D-3D Sphere-Cube Phantom

We start the evaluation of the multi-modal 2D-3D non-rigid registration algorithm with a simple 2D-3D sphere-cube phantom (SCP) with a homogeneous background (no soft tissue simulated) and analyse the robustness of the reconstructed dissimilarity $D_{\boldsymbol{u}}^{R}(\boldsymbol{x})$ against different Poisson noise level. The result of the deformed cube after registration and corresponding noisy DRRs (disturbed by different noise levels) is shown in Fig. 2.

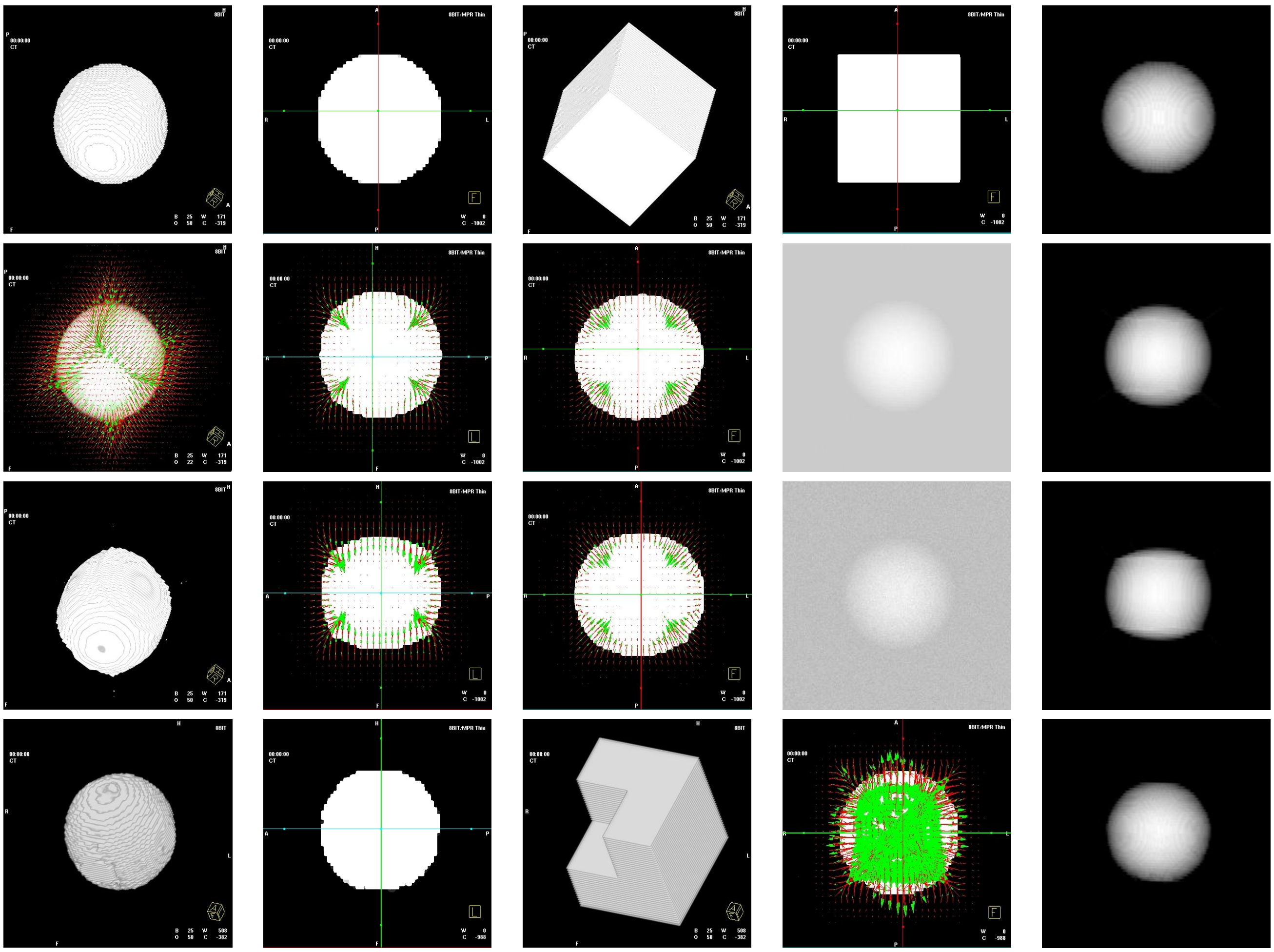

Figure 2. Sphere-Cube phantom (from top left): VRT of GT, MPR-F of GT, VRT and MPR-F of the template before alignment, DRR of GT; 2nd row (result of case 1.1): VRT with $\boldsymbol{u}$, MPR-L with $\boldsymbol{u}$, MPR-F with $\boldsymbol{u}$, one of the noisy $\boldsymbol{r}^{\phi}$ (DRRs) used for alignment, corresponding DRR after alignment; 3rd row (result of case 1.2): VRT, MPR-L with $\boldsymbol{u}$, MPR-F with $\boldsymbol{u}$, noisy $\boldsymbol{r}^{\phi}$ (DRR) used for alignment, corresponding DRR after alignment; 4th row (result of case 1.3): VRT, MPR-L after alignment, VRT before alignment, MPR-F with computed $\boldsymbol{u}$ and DRR after alignment. In case 1.1 the deformed 3D cube becomes very close to the GT sphere. In case 1.2 leads the stronger Poisson noise compared to case 1.1 to a less curved deformation of the cube. The missing corner of the cube template (4th row) is also well aligned to a sphere like in case 1.1.

4.2. SphereHelix Phantom

The SphereHelix phantom (top left image in Fig. 3) consists of spheres (constant intensity of 0.9) aligned along a helical trajectory with decreasing sphere and helix radius. Soft-tissue (intensity range [0, 0.3]) is simulated via uniformly distributed noise in the image background. The phantom is finally filtered with a gaussian kernel. The non-rigid deformed phantom, shown in Fig. 3 (left image in 2nd row), is aligned with its DRRs computed before the deformation. The experimental cases and results are shown in Fig. 4.

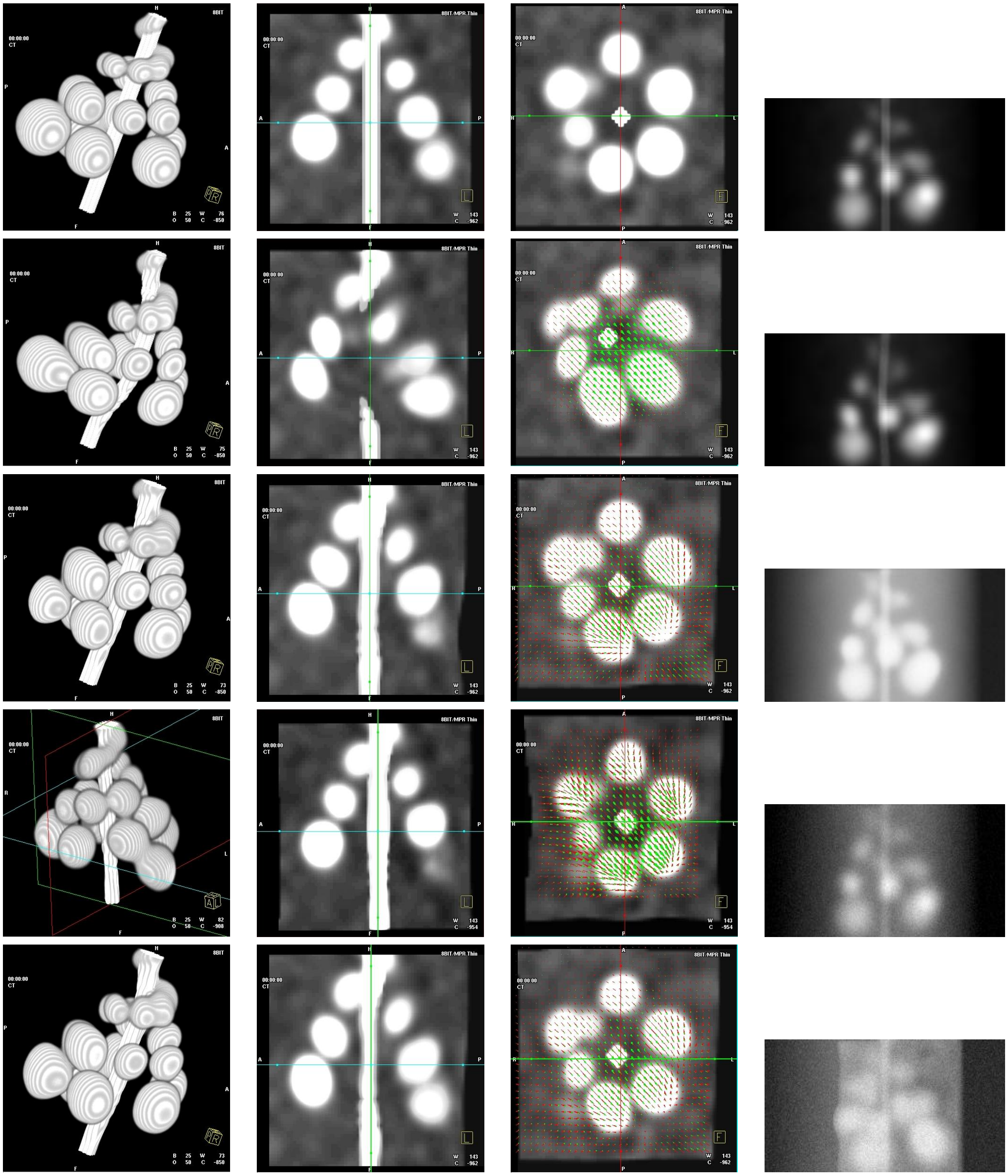

Figure 3. SphereHelix phantom: The ground truth phantom via VRT, MPR-L, MPR-F and one of the computed DRRs ($\boldsymbol{r}^{\phi}$, no noise) is shown in the 1st row. The VRT, MPR-L, MPR-F with ground truth deformation field $\boldsymbol{u}$ and DRR of the deformed GT ($\boldsymbol{t}$) is shown in the 2nd row. In the 3rd, 4th and 5th row is respectively case 2.1, 2.2 and 2.3 shown via VRT, MPR-L, MPR-F with computed $\boldsymbol{u}$ and one of the used DRRs ($\boldsymbol{r}^{\phi}$, with noise). The deformed stick along the center axis of the phantom is moved back to the center after the alignment in each of the three cases. In the MPR-F is respectively the computed non-rigid squarish looking $\boldsymbol{u}$ shown. In case 2.2 is the IK projector used which provides a smoother alignment where the center stick is less deformed along its outer contour compared to the cases 2.1 and 2.2 where the AC projector is used. The histograms of all computed and for the alignment used DRRs are equalized and scaled to the range [0, 1024].

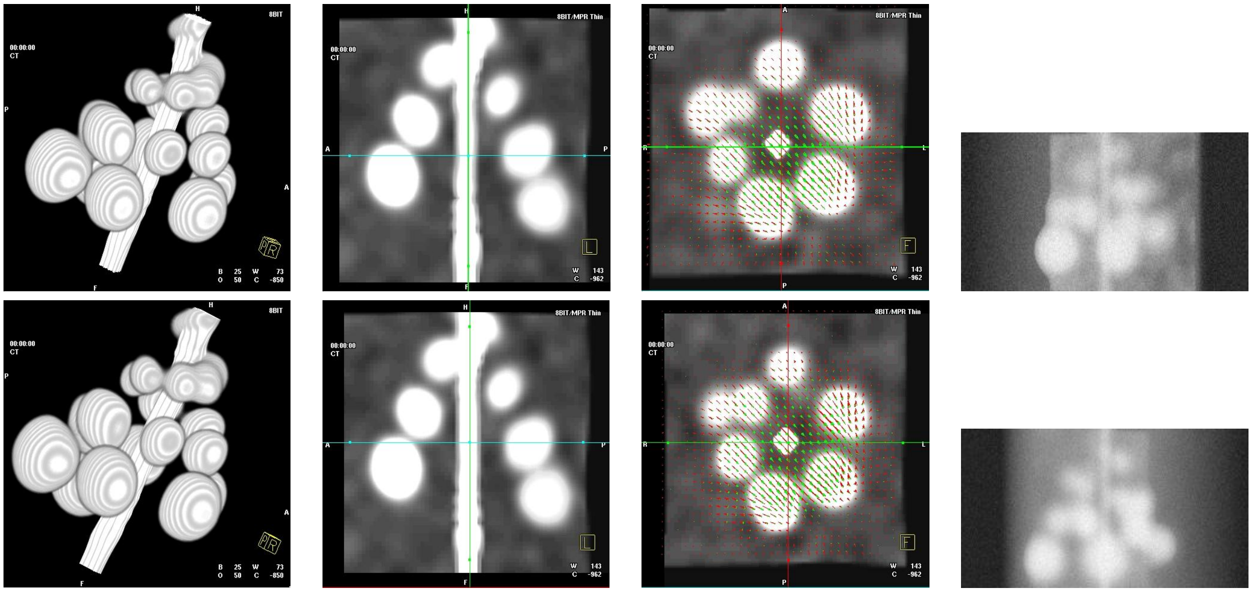

Figure 4. SphereHelix phantom: Case 2.4 and 2.4 is respectively shown in the 1rd and 2nd row via VRT, MPR-L, MPR-F with computed $\boldsymbol{u}$ and one of the used DRRs ($\boldsymbol{r}^{\phi}$, with noise). In case 2.4 a less curvatured $\boldsymbol{u}$ is allowed compared to case 2.5 (see Table 1) and also stronger Poisson noise is added to the computed DRRs used for the alignment.

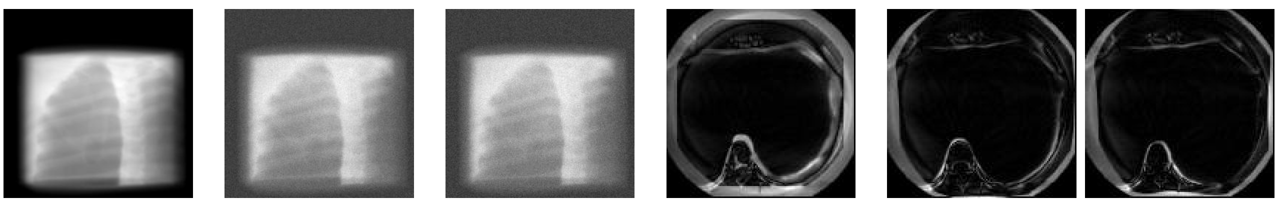

Figure 5. C-arm CT thorax image. The GT thorax image is deformed via non-rigid sinuodal deformation that actually shrinks the thorax image before alignment. From left to right: computed DRR without noise, noisy DRR of case 3.1 and case 3.2, difference image of the center volume slice (CVS) between the GT and the deformed thorax image before alignment, difference image of CVS of case 3.1 and case 3.2 after alignment. In case 3.2 is stronger Poisson noise added to the DRRs used for the alignment. The backbone and chest is moved back close to its location before the artificial deformation.

4.3. C-arm CT Image

Two test cases are shown (Fig. 6 and Fig. 5) using a real C-arm CT thorax image. A non-rigid (sinuodal) synthetic deformation was added to the thorax image to simulate breathing of a patient. The GT thorax image represents the thorax after breath in and the template image after exhalation. The computed projection images used for alignment are also histogram equalized and disturbed by Poisson noise.

5. SUMMARY AND DISCUSSION

A new multi-modal non-rigid 2D-3D registration technique is presented. It allows the registration of pre-operatively reconstructed 3D C-arm CT images with intra-intervetionally acquired noisy X-ray images (fluoroscopies). The benefit of this 2D-3D registration approach is its scalability in the number of used 2D reference images. Although it makes less sense to register the volume with only one X-ray image, the registration algorithm can already be started with one X-ray image. Subsequently acquired intraoperative X-ray reference images can be added successively during the intervention. The more reference images, uniformly spread around 180 degree, are used for registration the more accurate and smooth the non-rigid transformation will be.

Using component averaged back-projection of the variational gradient functional of MI generates a signed 3D distance that can be introduced into the 3D-3D registration framework to compute a smooth non-rigid 3D transformation.

The non-rigid registration can only deal with small deformations, e.g. breathing of a patient. If the orientation of the high contrast 3D image is unknown a rigid 2D-3D registration should be applied before the 2D-3D non-rigid alignment. Using interpolation kernels for the projector provides a much smoother MRCAV distance with less artifacts in the 3D reconstructed variational gradient functional.

This 2D-3D registration approach allows an efficient implementation. Mapping e.g. a mean relaxation of the SART[18] algorithm on graphics hardware to back-project the dissimilarity into 3D and using a fast DCT-technique introduced by Fischer, Modersitzki *et. al.*[15] to solve the Euler-Lagrange equation (3), the algorithm becomes capable for clinical applications. Furthermore the forward and backward projector for MRCAV does not have necessarily the same. For the forward projection of the deformed volume $\boldsymbol{t_u}$ a fast volume rendering technique using transfer functions can be applied. The parameters of the transfer function are used to identify the voxel intensities that are considered for registration as introduced by Hahn[3] *et. al.*. The existing 2D-3D non-rigid registration algorithms are not runtime optimized and only part of a scientific framework available at the University of Erlangen-Nuremberg, Germany.

6. ACKNOWLEDGEMENTS

We would like to thank Siemens Medical Solutions for providing C-arm CT images (Siemens Axiom-Artis) for 2D-3D registration. The authors gratefully acknowledge the support of Deutsche Forschungsgemeinschaft (DFG) under the grant SFB 603, TP, C10. The authors are also thankful to HipGraphics for providing the volume rendering software (InSpace).

Case	Iterations	Φ	μ	*Proj.*	α	τ	BINS	$\epsilon^{dis}_{bef.}$	$\epsilon^{dis}_{aft.}$	time (min)
1.1	20	9	10	AC	0.6	1.7	25	0.943928	0.310622	2
1.2	40	9	500	AC	0.1	3.0	30	0.943928	0.399099	4
1.3	40	10	5	AC	0.01	6.0	25	0.967389	0.475514	4
2.1	30	12	50	AC	2.5	150	25	0.651297	0.454372	3
2.2	90	13	1200	IK	0.09	400.0	25	0.651297	0.435077	120
2.3	60	19	1500	AC	3.0	100.0	25	0.651297	0.407933	7
2.4	40	45	1000	AC	2.0	35.0	25	0.651297	0.386791	12
2.5	80	45	500	AC	0.9	20.0	25	0.651297	0.378900	24
3.1	30	16	800	AC	15.0	20.0	25	1.053216	0.583662	10
3.2	40	16	1300	AC	15.0	20.0	25	1.053216	0.543920	15

Table 1. Parameter setting and results of the Sphere-Cube phantom (case 1.x; 2D: $256\times256\times\Phi$, 3D: $64\times64\times64$), Sphere-Helix phantom (case 2.x; size 2D: $256\times128\times\Phi$, 3D: $64\times64\times64$) and C-arm CT data (case 3.x; size 2D: $256\times256\times\Phi$, 3D: $128\times128\times128$). The table shows the result in dependency of the number of used X-ray images Φ, Poisson noise strength μ, used projector for MRCAV, curvature regularization α, time-step τ, used BINS for the joint-histogram and the error distance ϵ^{dis}(15) between the aligned 3D image and the GT before and after alignment. Hardware: Intel Pentium 3GHz.

REFERENCES

1. Prümmer M., Han J., Hornegger J., *2D-3D Non-rigid Registration using Iterative Reconstruction*, Workshop Vision Modeling and Visualization in Erlangen, Germany 2005, http: www.vmv2005.uni-erlangen.de, vol 1, ISBN 3-89838-068-8, p. 187-194.
2. Hermosillo, G., Chefd' Hotel C., Faugeras, O., *Variational Methods for Multimodal Image Matching*, Int. J. Comput. Vision, vol. 50, no. 3, 2002, ISSN 0920-5691, p. 329–343, Kluwer Academic Publishers.
3. Hahn, D. A. and Hornegger, J. and Bautz, W. and Kuwert, T. and Römer, W., "*Unbiased rigid registration using transfer functions*", *Proc. of SPIE on Medical Imaging 2005*, vol. 5747, p. 151-162.

4. Gueziec, A., "*Assessing the registration of CT-scan data to intraoperative x-rays by fusing x-rays and pre-operative information*", *Proceding SPIE Medical Imaging'99*, p. 3661-3688.
5. Feldmar, J., N. Ayache and F. Betting, "*3D-2D projective registration of free–from curves and surfaces*", 1994, INRIA, France.
6. Hamadeh, A., et. al., "*Towards automatic registration between CT and X-ray images: cooperation between 3D/2D registration and 2D edge detection*", in 2nd Annual Internaltional Symposium on MRCAS, 1995. Baltimore, MD USA.
7. Weese, J., et. al. "*An Approach to 2D/3D Registration of a Vertebra in 2D X-ray Fluoroscopes with 3D CT Images*", in Computer Vision and Virtual Reality in Medicine II - Medical Robotics and Computer Assisted Surgery III, 1997, France.
8. LaRose, D., "*Iterative X-ray/CT registration using accelerated volume rendering*", in Robotics Institute, 2001, Carnegie Mellon University.
9. Zollei, L., "*2D-3D rigid registration of X-ray fluoroscopy and CT images using mutual information and sparsely sampled histogram estimators*", in IEEE CVPR, 2001.
10. Yao, J., et. al. "*Assessing accuracy factors in deformable 2D/3D medical image registration using a statistical Pelvis model*", in Proceedings of the Ninth IEEE International Conference on Computer Vision (ICCV 2003) 2-Volume.
11. Broit, C. *Optimal registration of deformed images*, Ph.D Thesis, Computer and Information Science, Uni Pensylvania, 1981.
12. Morten, B., *Medical image registration and surgery simulation*, Ph.D Thesis, IMM, Technical University of Denmark, 1996.
13. Christensen, G., *Deformable shape models for anatomy*, Ph.D Thesis, Sever Institute of Technology, Washington University, 1994.
14. Fischer, B. and Modersitzki, J. *Fast diffustion registration*, AMS contemporary Mathematics, Inverse Problems, Image Analysis, and Medical Imaging, vol. 313, 2002, pp: 117-129.
15. Fisher. B and J. Modersitzki, "*Curvature based image registration*", JMIV 18(1), 2003.
16. Y. Censor and T. Elfving, "*Block-Iterative Algorithms with Diagonally Scaled Oblique Projections for the Linear Feasibility Problem*", SIAM Journal on Matrix Analysis and Applications, vol. 24, number 1, p. 40-58, 2002.
17. Y. Censor and D. Gordon and R. Gordon, "*Component averaging: An efficient iterative parallel algorithm for large and sparse unstructured problems*", Parallel Computing, vol. 27, pp. 777-808, 2001.
18. K. Mueller and R. Yagel and J. J. Wheller, "*Fast Implementation of Algebraic Methods for 3D Reconstruction from Cone-Beam Data*", IEEE Trans. Med. Imaging, Vol. 18, No. 6, pp. 538-548, 1999.
19. J. D. Foley and A. van Dam and S. K. Feiner and J. F. Hughes, "*Computer Graphics: Principles and Practice in C*", isbn 0201848406, 1995, Addison-Wesley Professional.
20. M .Jiang, G. Wang, "*Convergence studies on iterative algorithms for image reconstruction*", IEEE Trans Med Imaging. 2003 May, Vol. 22 No. 5, pp. 569-79.
21. M .Jiang, G. Wang, "*Development of iterative algorithms for image reconstruction*", Journal of X-Ray Science and Technology Vol. 10, 2002, pp. 77-86, IOS Press.
22. P. E. Danielsson and M. Magnusson Seger "*Combining Fourier and iterative methods in computer tomography. Analysis of an iteration scheme. The 2D-case*", Dept. EE, Linköping University, Oct. 2004, No. LiTH-ISY-R-2634, SE-581 83 Linköping, Sweden.
23. S. Jonić, P. Thévenaz, M. Unser "*Multiresolution Spline-Based 3D/2D Registration of CT Volume and C-Arm Images for Computer-Assisted Surgery*", Proceedings of the SPIE International Symposium on Medical Imaging, San Diego CA, USA, February 17-22, 2001, vol. 4322, Part II, pp. 1101-1109.

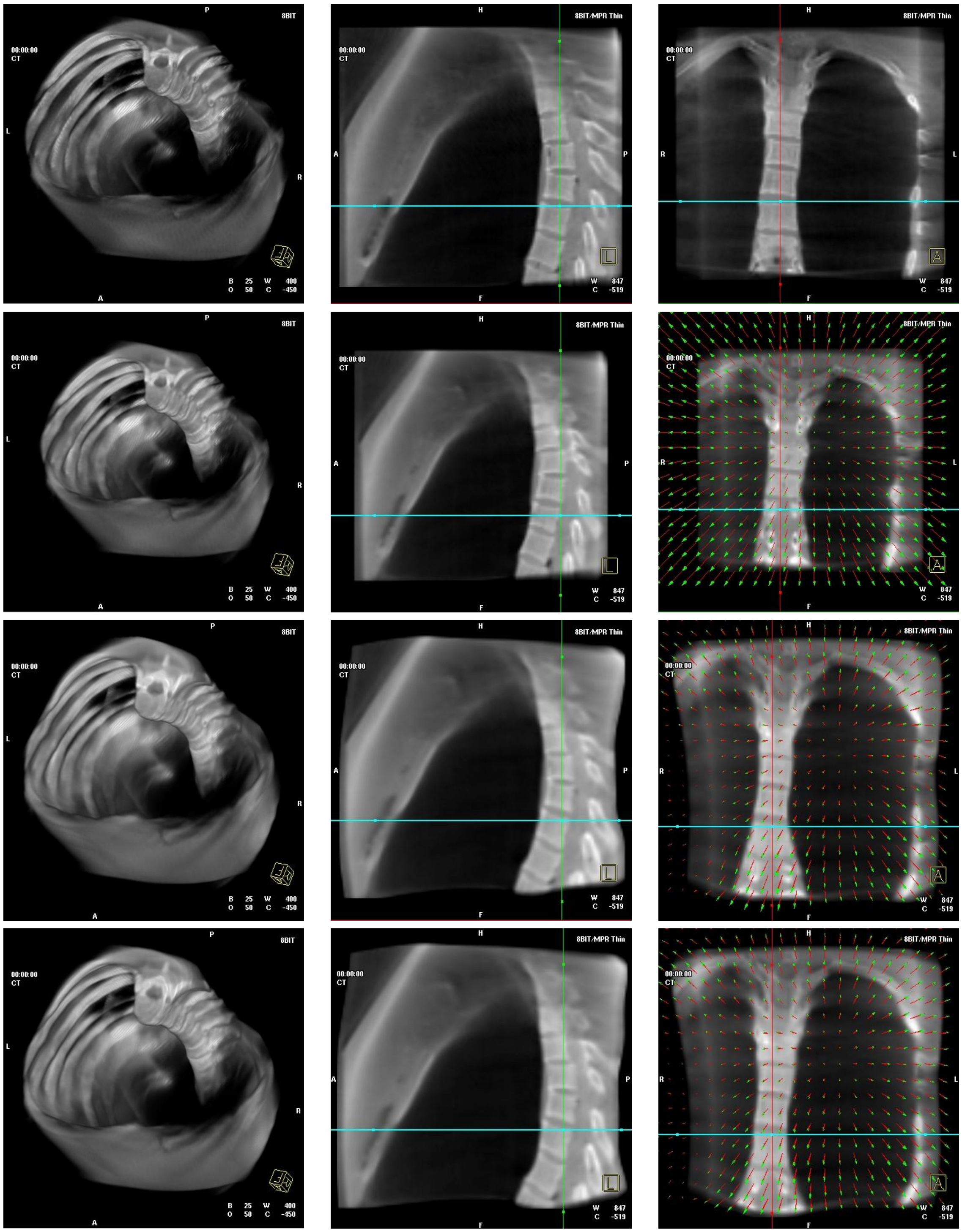

Figure 6. C-arm CT thorax image. 1st row: GT thorax image shown via VRT, MPR-L and MPR-A. 2nd row: artificial deformed thorax image with non-rigid sinuodal deformation that shrinks the thorax image. Shown via VRT, MPR-L and MPR-A with ground truth deformation field $\boldsymbol{u}$. 3rd row: result of case 3.1 shown via VRT, MPR-L and MPR-A with computed deformation field $\boldsymbol{u}$ after alignment. 4th row: result of case 3.2 shown via VRT, MPR-L and MPR-A with computed deformation field $\boldsymbol{u}$ after alignment. The computed deformation $\boldsymbol{u}$ represents in both cases the shown ground truth deformation in the 2nd row. In case 3.2 the backbone is less curved after alignment compared to case 3.1 applying more iterations, but also stronger Poisson noise disturbed DRRs.